Monthly Notices of the ROYAL ASTRONOMICAL SOCIETY
MNRAS **496,** 1959–1966 (2020)
Advance Access publication 2020 June 5
doi:10.1093/mnras/staa1578

Prospects for cosmic magnification measurements using H I intensity mapping

Amadeus Witzemann,[1★] Alkistis Pourtsidou[1,2] and Mario G. Santos[1,3]
[1]*Department of Physics and Astronomy, University of the Western Cape, Cape Town 7535, South Africa*
[2]*School of Physics and Astronomy, Queen Mary University of London, Mile End Road, London E1 4NS, UK*
[3]*South African Radio Astronomy Observatory (SARAO), 2 Fir Street, Observatory, Cape Town 7925, South Africa*

Accepted 2020 May 28. Received 2020 May 27; in original form 2019 July 1

ABSTRACT
We investigate the prospects of measuring the cosmic magnification effect by cross-correlating neutral hydrogen intensity mapping (H I IM) maps with background optical galaxies. We forecast the signal-to-noise ratio for H i IM data from SKA1-MID and HIRAX, combined with LSST photometric galaxy samples. We find that, thanks to their different resolutions, SKA1-MID and HIRAX are highly complementary in such an analysis. We predict that SKA1-MID can achieve a detection with a signal-to-noise ratio of ∼15 on a multipole range of $\ell \lesssim 200$, while HIRAX can reach a signal-to-noise ratio of ∼50 on $200 < \ell < 2000$. We conclude that measurements of the cosmic magnification signal will be possible on a wide redshift range with foreground H I intensity maps up to $z \lesssim 2$, while optimal results are obtained when $0.6 \lesssim z \lesssim 1.3$. Finally, we perform a signal to noise analysis that shows how these measurements can constrain the H I parameters across a wide redshift range.

Key words: gravitational lensing: weak – large-scale structure of Universe.

1 INTRODUCTION

Travelling through the Universe, the path of light is deflected by the mass distribution it encounters. Images of distant light sources are distorted by the intervening matter along the line of sight (LOS), an effect well described by General Relativity. As a result, distortions of shapes, magnifications, and even duplicate images are observed and are generally classified as weak or strong gravitational lensing.

Weak gravitational lensing or cosmic shear is a coherent distortion of the shapes of galaxies, and has been routinely detected using optical galaxy surveys, with the first detections reported almost two decades ago (see, for example, Bacon, Refregier & Ellis 2000; Kaiser, Wilson & Luppino 2000; van Waerbeke et al. 2000; Wittman et al. 2000). Ongoing and forthcoming large-scale structure surveys like CFHTLens (Heymans et al. 2012), DES (Abbott et al. 2016), *Euclid* (Amendola et al. 2018), and LSST (Abate et al. 2012), will give precise cosmic shear measurements and use them to constrain the properties of dark energy. The accuracy and robustness of weak lensing measurements depends on the control of various systematic effects such as intrinsic alignments, point spread function, seeing and extinction, as well as photometric redshift calibration (Mandelbaum 2018). In addition, Stage IV lensing surveys with *Euclid* and LSST will need accurate theoretical modelling of non-linear clustering and baryonic effects down to very small scales to achieve their goals. Further improvements will come from the use of galaxy–galaxy lensing cross correlations (van Uitert et al. 2018).

In addition to the distortion of galaxy shapes, there is another form of lensing, cosmic magnification, which can be measured even when the sizes and shapes of sources are inaccessible. This makes it particularly attractive as it is free from many systematics such as the point spread function and intrinsic alignments (see, for example, Zhang & Pen (2006), which discussed the possibility of using radio galaxy surveys to detect this effect). Magnification occurs when intervening structure between an observer and a source acts to magnify or demagnify the object, i.e. sometimes allowing the observer to see objects otherwise too faint (Bartelmann & Schneider 2001). However, the apparent observed area can also be increased, which leads to an apparent decrease in number counts if the total number is conserved. Only slightly altering the observed structures, this effect is notoriously difficult to measure (see e.g. the discussion in Hildebrandt, van Waerbeke & Erben 2009). Several promising techniques exist, but there have been only a few, and controversial, detections (see discussion and references in Scranton et al. 2005). The first time this signal was measured with high significance was the 8σ detection achieved in Scranton et al. (2005) using the Sloan Digital Sky Survey and the galaxy–quasar cross-correlation. A more recent analysis with DES galaxies is presented in Garcia-Fernandez et al. (2018).

Measurements of cosmic magnification probe the galaxy halo occupation distribution, dark matter halo ellipticities, and the extent of galaxy dust haloes (Scranton et al. 2005; Menard et al. 2010) – they are complementary to shear–shear measurements, and they can be used to break parameter degeneracies (Van Waerbeke et al. 2010). Similar to cosmic shear, cosmic magnification provides constraints

★ E-mail: amadeus.witzemann@gmx.at

on the galaxy–matter correlation, but without the requirement of measuring shapes, it suffers from less systematic errors and can be extended to sources at much higher redshifts (Scranton et al. 2005). In addition to probing the matter distribution directly, magnification also plays an important role in *geometrical methods* to measure dark energy parameters independently of the matter power spectrum (Jain & Taylor 2003; Bernstein & Jain 2004; Taylor et al. 2007). These methods use galaxy-lensing correlations and therefore depend on estimates of the galaxy density. This is directly affected by magnification, which can therefore introduce systematic errors unless corrected for (Scranton et al. 2005; Hui, Gaztañaga & Loverde 2007; Ziour & Hui 2008; Bonvin & Durrer 2011).

A straightforward approach to measure magnification uses the angular cross-correlation between foreground and background galaxy counts (see e.g. Hildebrandt et al. 2009), where galaxy-magnification or magnification–magnification cross correlations would be major contributors to a non-zero signal.

Following a similar line of thought, we propose to use H I intensity maps acting as foreground lenses, magnifying a background distribution of galaxies. A motivation for using H I is that intensity maps have no lensing corrections at first order due to flux conservation (Hall, Bonvin & Challinor 2013), which removes magnification–magnification correlations between foreground and background. This potentially decreases the signal, but also helps interpretation by removing additional terms in the signal calculation. In addition, the excellent redshift resolution of the foreground H I maps allows to combine measurements using different slices of the H I distribution. Using H I intensity maps also mitigates the danger of overlapping foreground and background sources, which results to a clustering (not lensing) signal. Furthermore, radio and optical observations are subject to different systematic effects, which are expected to drop out in cross correlation. In the following, we derive forecasts for a potential detection of the magnification signal, using noise properties for the planned radio telescopes SKA1-MID (Bacon et al. 2020) and HIRAX (Newburgh et al. 2016), as well as LSST.

The plan of the paper is as follows: In Section 2 we give an introduction to cosmic magnification statistics and introduce the possibility of using H I intensity maps as foreground lenses. In Section 3 we calculate the instrumental (thermal) noise of SKA1-MID and HIRAX, as well as the shot noise from the LSST sample, and investigate the signal and noise properties for the cosmic magnification measurement. In subsection 4.1, we optimize the signal-to-noise ratio for our proposed method and derive the cumulative signal-to-noise ratio for SKA1-MID and HIRAX. In subsection 4.2, we present constraints on the cumulative signal-to-noise ratio using a weighted galaxy overdensity, which turns out to predict a better signal to noise. We also turn these constraints into fractional error forecasts on $\Omega_{\rm HI}b_{\rm HI}$. We summarize our findings and conclude in Section 5.

2 COSMIC MAGNIFICATION STATISTICS

In this section we describe the power spectrum formalism for measuring the cosmic magnification signal from background galaxies. We start with the standard approach, which assumes a galaxy sample as the foreground sample, and then introduce the possibility of using H I intensity maps instead.

2.1 Galaxies as the foreground sample

Galaxies are biased tracers of the underlying dark matter distribution, which is thought to contain most of the mass distributed along the LOS to a light source. Magnification will increase the flux from a galaxy, making it appear brighter than it actually is. Therefore galaxies normally too faint to be detected can still be seen if the magnification caused by the matter along the LOS is strong enough. However, the apparent area of a source is also increased, resulting in a decrease of the observed number density of galaxies. We can write (Zhang & Pen 2006)

$$\delta_{\rm g}^{\rm L} = \delta_{\rm g} + (5s_{\rm g} - 2)\kappa + \mathcal{O}(\kappa^2), \tag{1}$$

with $\delta_{\rm g}^{\rm L}$ and $\delta_{\rm g}$ the lensed and unlensed intrinsic galaxy overdensities, respectively, and κ the lensing convergence. For a survey with limiting magnitude $m^\star$ the number count slope $s_{\rm g}$ is given by (Duncan et al. 2014)

$$s_{\rm g} = \frac{d\,\log_{10} n_{\rm g}(< m^\star)}{dm^\star}, \tag{2}$$

with the cumulative number of detected galaxies per redshift interval and unit solid angle, $n_{\rm g}$. The cross-correlation of well-separated foreground (at position $\theta_{\rm f}$ and redshift $z_{\rm f}$) and background ($\theta_{\rm b}$ and $z_{\rm b}$) galaxy samples is free from the intrinsic galaxy overdensity correlation term $\langle\delta_{\rm g}(\theta_{\rm f}, z_{\rm f})\delta_{\rm g}(\theta_{\rm b}, z_{\rm b})\rangle$, therefore

$$\left\langle \delta_{\rm g}^{\rm L}(\theta_{\rm f}, z_{\rm f})\delta_{\rm g}^{\rm L}(\theta_{\rm b}, z_{\rm b})\right\rangle = \left\langle \left(5s_{\rm g}^{\rm b} - 2\right)\kappa_{\rm b}\delta_{\rm g}(\theta_{\rm f}, z_{\rm f})\right\rangle + \left\langle \left(5s_{\rm g}^{\rm f} - 2\right)\left(5s_{\rm g}^{\rm b} - 2\right)\kappa_{\rm f}\kappa_{\rm b}\right\rangle, \tag{3}$$

where the superscript L denotes lensed quantities. The right-hand side of equation (3) contains the magnification–galaxy ($\mu - {\rm g}$) correlation (first term) and the magnification–magnification ($\mu - \mu$) correlation (second term). The latter is subdominant for foregrounds at comparably low redshifts and therefore usually neglected. If both foreground and background galaxies are at high redshifts, however, it can become large (Ziour & Hui 2008).

2.2 H I intensity maps as the foreground sample

In this work, we focus on the magnification effect of H I intensity maps in the foreground, acting on the clustering statistics of background galaxies. Intensity maps themselves are not lensed at linear order due to surface brightness conservation (Hall et al. 2013). Intensity mapping lensing is very similar to CMB lensing, and a technique for measuring gravitational lensing in 21 cm intensity mapping observations of H I after reionization was developed in Pourtsidou & Metcalf (2014), building upon previous work by Zahn & Zaldarriaga (2006). In later studies, higher order effects were included. For example Jalilvand et al. (2019) calculated the second-order lensing effects on the intensity mapping power spectrum at $z = 2 - 6$. They computed the corrections by Taylor-expanding in the deflection angle up to second order and found an extra term that can be important at high redshifts.

To summarize, while the notion of number counts is not relevant for H I intensity mapping, the absence of lensing at linear order is formally equivalent to setting $s_{\rm H\,I} = 2/5$. We also have

$$\delta T_{21}^{\rm L} = \delta T_{21} = \bar{T}_{21}\delta_{\rm HI} = \bar{T}_{21}b_{\rm HI}\delta, \tag{4}$$

where $\bar{T}_{21}$ is the mean brightness temperature of neutral hydrogen, $b_{\rm H\,I}$ is the hydrogen bias and δ the dark matter overdensity. Considering galaxies as the background sample, we now have

$$\left\langle \delta_{\rm HI}^{\rm L}(\theta_{\rm f}, z_{\rm f})\delta_{\rm g}^{\rm L}(\theta_b, z_b)\right\rangle = \left\langle \left(5s_{\rm g}^{\rm b} - 2\right)\kappa_b b_{\rm HI}\delta(\theta_{\rm f}, z_{\rm f})\right\rangle, \tag{5}$$

where the magnification–magnification term is absent since $s_{\rm H\,I} = 2/5$. The above relation holds at all redshifts, given that the foreground and background samples are well separated. This can be guaranteed via the excellent redshift information provided by the intensity mapping survey.

The observable magnification signal can be expressed using the angular power spectrum (Zhang & Pen 2006; Ziour & Hui 2008)

$$C_\ell^{\mathrm{HI}-\mu}(z_\mathrm{f}, z_\mathrm{b}) = \frac{3}{2}\frac{H_0^2}{c^2}\Omega_{\mathrm{m},0} \times \int_0^\infty dz \frac{b_\mathrm{HI}\bar{T}_{21}(z)W(z,z_\mathrm{f})g(z,z_\mathrm{b})}{r^2(z)}(1+z) \times P_\mathrm{m}((\ell+1/2)/r(z), z), \quad (6)$$

where $r(z)$ is the comoving distance to redshift z and we have applied the Limber approximation, valid for $\ell \geq 10$ (Limber 1954; Loverde & Afshordi 2008). The redshift distribution of the foreground H I intensity maps is given by a top hat over the foreground redshift bin $W(z, z_\mathrm{f})$ and $g(z, z_\mathrm{b})$ is the lensing kernel:

$$g(z, z_\mathrm{b}) = \frac{r(z)}{N_\mathrm{g}(z_\mathrm{b})}\int_{z_\mathrm{b}^\mathrm{min}}^{z_\mathrm{b}^\mathrm{max}} \mathrm{d}z' \frac{r(z')-r(z)}{r(z')}(5s_\mathrm{g}(z')-2)n_\mathrm{g}(z'), \quad (7)$$

where the average number of galaxies per square degree in the background bin is

$$N_\mathrm{g}(z_\mathrm{b}) \equiv \int_{z_\mathrm{b}^\mathrm{min}}^{z_\mathrm{b}^\mathrm{max}} n_\mathrm{g}(z)\mathrm{d}z, \quad (8)$$

and $z_\mathrm{b}^\mathrm{min}$, $z_\mathrm{b}^\mathrm{max}$ denote the minimum and maximum redshift for the background galaxy sample. An interesting feature of the geometrical weight $\frac{r(z')-r(z)}{r(z')}$ is that, in a flat universe, it takes the form of a parabola with a maximum at $r(z') = r/2$. Thus, structures halfway between the source and the observer are the most efficient to generate lensing distortions (Kilbinger 2015) (and very low redshift foregrounds are less favoured).

For increased computational speed, we use a fitting function to approximate the cumulative galaxy count for LSST, n_g, provided in the publicly available code from Alonso et al. (2015). This code in turn uses the Schechter function (Schechter 1976) for the r'-band luminosity from Gabasch et al. (2006), with the faint end slope $\alpha = -1.33$, the characteristic magnitude M^*

$$M_*(z) = M_0 + a\ln(1+z) \quad (9)$$

and the density ϕ^*

$$\phi_*(z) = (\phi_0 + \phi_1 z + \phi_2 z^2)[10^{-3}\mathrm{Mpc}^{-3}]. \quad (10)$$

Here $M_0 = -21.49$, $a = -1.25$, $\phi_0 = 2.59$, $\phi_1 = -0.136$, $\phi_2 = -0.081$. We adapt the fit from LSST Science Collaboration (2009) to approximate n_g as follows,

$$n_\mathrm{g}(z) \propto z^\alpha \exp\left(-\left(\frac{z}{z^*}\right)^\beta\right), \quad (11)$$

where we optimize the parameters α, β, and z^* to fit n_g from Alonso et al. (2015) as functions of magnitude cutoff m^* by interpolation. Fig. 1 compares this fit with the true n_g and with several other fitting functions. The overall amplitude is irrelevant in equation (7), as n_g is normalized to integrate to one, but it is required to calculate the shot noise – see Section 3 for details.

The number count slope s_g (Fig. 2) rises quicker for a lower magnitude cutoff, therefore the magnitude threshold can be chosen to avoid a sign change of $5s_\mathrm{g} - 2$ in the background redshift bin. The amplitude of the magnification signal is proportional to a redshift integral of $5s_\mathrm{g} - 2$ (equations 2 and 6). An appropriate magnitude cutoff thus boosts the signal by avoiding cancellations inside the integral for the lensing kernel g. Fig. 2 demonstrates this in a situation where a lower magnitude threshold is beneficial to optimize the magnification signal, which is shown in Fig. 3. Decreasing m^* comes at the cost of a smaller number of observed galaxies and therefore increased shot noise. We optimize to achieve a maximal signal to noise ratio. We will further discuss this in Section 3.2, and we also note that a number count slope weighting was suggested in Menard & Bartelmann (2002) and used in the SDSS data analysis of Scranton et al. (2005).

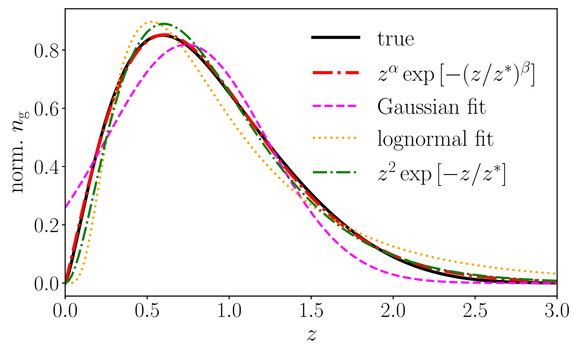

Figure 1. Different fitting functions for the cumulative galaxy number count were considered. The normalized 'true' function here is taken from Alonso et al. (2015) (solid black line). The best fitting function (red dotted-dashed line) is given in equation (11).

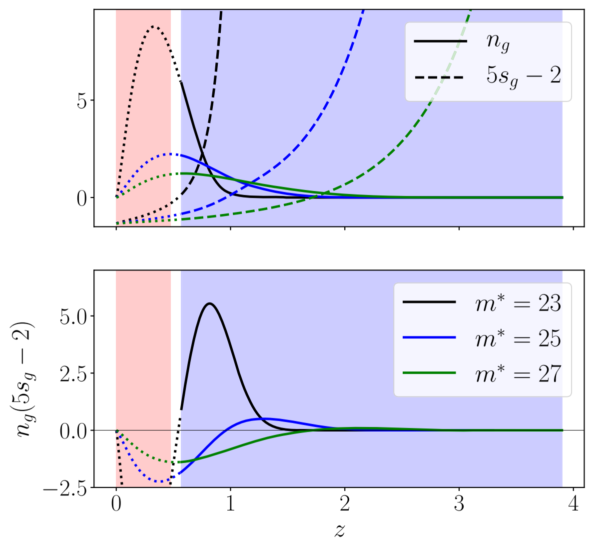

Figure 2. We illustrate the behaviour of the number count slope s_g and galaxy count n_g with respect to the magnitude threshold m^*, here with foreground redshift $0 < z < 0.47$, which corresponds to band 2 of SKA1-MID, described in detail in Section 3. The red (blue) shaded areas indicate the foreground (background) redshift range. The upper panel displays the galaxy number density n_g (normalized to integrate to one inside the background bin), and the contribution of the number count slope s_g. The bottom panel shows the product $n_\mathrm{g}(5s_\mathrm{g} - 2)$, which is the only term inside the integral equation (7) to potentially be negative. This demagnification leads to cancellation in the integration and thus to a smaller lensing signal. An appropriate magnitude cutoff enforces $5s_\mathrm{g} > 2$ in the background redshift bin and thus boosts the signal. However, this comes at the cost of increasing the galaxy shot noise.

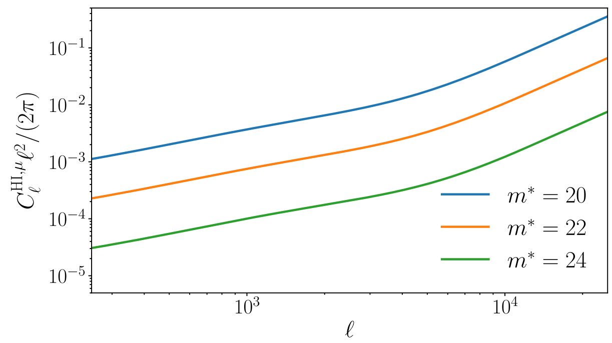

Figure 3. The H I magnification cross-correlation power spectrum for a foreground redshift from $z = 0$ to 0.47, corresponding to band 2 of SKA1-MID. Lower magnitude cuts increase the magnification signal.

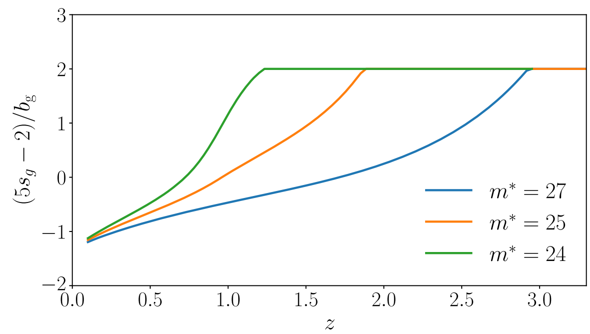

Figure 4. The ratio of number count slope and galaxy bias $(5s_{\mathrm{g}} - 2)/b_{\mathrm{g}}$ for different magnitude cutoff values. This sample dependent ratio describes the relative importance of clustering and magnification. It is set to 2 for higher redshifts via the choice of galaxy bias, see equation (17). This choice has a negligible effect on our results, as it affects a regime where the number of galaxies quickly approaches zero. The maximum magnitude detectable with LSST is assumed to be 27. Imposing a lower magnitude cutoff increases the shot noise, but also the number count slope, which increases the magnification signal.

We use CAMB with HALOFIT (Lewis, Challinor & Lasenby 2000; Smith et al. 2003; Takahashi et al. 2012) to estimate the non-linear matter power spectrum, $P_{\mathrm{m}}(k, z)$, assuming a flat ΛCDM cosmology with $h = 0.678$, $\Omega_c h^2 = 0.119$, $\Omega_b h^2 = 0.022$, $n_{\mathrm{s}} = 0.968$ (Aghanim et al. 2018).

The error in the measurement of the cross-correlation power spectrum is

$$\Delta C_\ell^{\mathrm{HI}-\mu} = \sqrt{\frac{2\left(\left(C_\ell^{\mathrm{HI}-\mu}\right)^2 + \left(C_\ell^{\mathrm{gg}} + C^{\mathrm{shot}}\right)\left(C_\ell^{\mathrm{HI-HI}} + N_\ell\right)\right)}{(2\ell + 1)\Delta\ell f_{\mathrm{sky}}}}, \tag{12}$$

where C^{shot} is the galaxy shot noise power spectrum, N_ℓ is the thermal noise of the intensity mapping instrument, $\Delta\ell$ is the binning in multipole space, and f_{sky} is the fraction of sky area overlap of the H I and optical surveys.

For the foreground H I IM sample we use a top-hat window function $W(z) = 1/\Delta z$ inside the bin of width Δz and zero elsewhere. We can then write the H I and galaxies autocorrelation power spectra as

$$C_\ell^{\mathrm{HI-HI}} = \frac{H_0}{c}\int \mathrm{d}z\, E(z)\left(\frac{b_{\mathrm{HI}}\bar{T}_{21}(z)W(z)}{r}\right)^2 P_{\mathrm{m}}\left(\frac{\ell + 1/2}{r}, z\right), \tag{13}$$

and

$$C_\ell^{\mathrm{g-g}} = \frac{H_0}{cN_{\mathrm{g}}^2}\int \mathrm{d}z\, E(z)\left(\frac{b_{\mathrm{g}}(z)n_{\mathrm{g}}(z)}{r}\right)^2 P_{\mathrm{m}}\left(\frac{\ell + 1/2}{r}, z\right), \tag{14}$$

where we have written the Hubble rate as $H(z) = H_0E(z)$, and the H I bias $b_{\mathrm{H\,I}}$ is given by fits to the results from Alonso et al. (2015):

$$b_{\mathrm{HI}}(z) = 0.67 + 0.18z + 0.05z^2. \tag{15}$$

The galaxy bias b_{g} naturally depends on redshift as well as magnitude cutoff, as brighter objects are rarer and thus more biased, an effect which is ignored when a simple linear and deterministic fitting function is used, for example

$$\tilde{b}_{\mathrm{g}}(z) = 1 + 0.84z. \tag{16}$$

To enforce a behaviour similar to that of the magnification bias at higher redshifts and more stringent magnitude cuts, we use a piecewise differentiable galaxy bias:

$$b_{\mathrm{g}}(z) = \max\left(\tilde{b}_{\mathrm{g}}, \frac{1}{2}(5s_{\mathrm{g}} - 2)\right). \tag{17}$$

This choice makes sure that the ratio $(5s_{\mathrm{g}} - 2)/b_{\mathrm{g}}$ converges for $n_{\mathrm{g}} \to 0$, as described in Hui et al. (2007). The value of this ratio depends on the selected sample, and it describes the relative importance of clustering and magnification. Measurements of the redshift dependence of the galaxy luminosity function can be used to derive constraints using the halo model (see e.g. Hui et al. 2007; Loverde, Hui & Gaztañaga 2007). In our forecasts, this ratio is shown in Fig. 4 for different magnitude cutoff values. As already mentioned, we are setting it to 2 for higher redshifts to avoid computational issues in a regime which is already heavily shot-noise dominated (Hui et al. 2007). We emphasize that while this choice is an assumption, it is a justified one – with a negligible effect on our analysis. The signal remains unaltered and (as will be shown) errors are mostly shot noise dominated.

The mean observed H I brightness temperature is calculated using the fit provided in Santos et al. (2017), which is based on the results from Santos et al. (2015):

$$\bar{T}_{21} = 0.0559 + 0.2324z - 0.024z^2\ \mathrm{mK}. \tag{18}$$

3 ERROR CALCULATIONS

3.1 H I intensity maps

We consider the experiments HIRAX and SKA1-MID to map the distribution of H I, used as the foreground sample. Together with the shot noise from LSST, their instrumental noise contributes to the total error budget given by equation (12).

HIRAX is a planned radio interferometer of 6 m diameter dishes, sharing the site in the Karoo in South Africa with MeerKAT and SKA1-MID. We assume the full planned array of 1024 and the reduced set of 512 dishes, arranged in a dense square grid with 1 m space between individual antennas. HIRAX aims to perform a large sky intensity mapping survey with 15 000 deg^2 area, and the integration time is taken to be two full years (corresponding to 4 yr observation). We assume a constant system temperature of 50 K on its entire frequency coverage ranging from 400 to 800 MHz (Newburgh et al. 2016).

At the same time, SKA1 is assumed to have only one year worth of integration time but a larger survey area of 16 900 deg^2.

This corresponds to the maximum possible survey overlap with LSST, after taking into account the total survey area of SKA1-MID (Santos et al. 2015) and contamination from galactic synchrotron radiation and dust. SKA1-MID will consist of different dish types: the (already operating) 64 MeerKAT dishes with 13.5 m, and 133 SKA1-MID dishes of 15 m diameter. For simplicity, we assume all dishes to be identical, taking an average dish diameter $\tilde{D}_{\rm dish} = (64 \times 13.5 + 133 \times 15)/(64 + 133)$ m and using a Gaussian beam pattern. We consider two observational bands: band 1 ranging from 350 to 1050 MHz, and band 2 from 950 to 1750 MHz (Bacon et al. 2020). The system temperature is assumed to be 30 K for band 1 and 20 K for band 2. This is conservative on low redshifts. For high-redshift foreground bins, the system temperature increases beyond that, but at the same time the galaxy shot noise becomes the dominant source of error and magnification detections quickly become extremely difficult for foreground samples with $z \gtrsim 2$. This justifies our assumption of constant system temperature for both SKA1-MID and HIRAX. For both experiments, we use equally spaced redshift bins of width $\Delta z = 0.5$, with the exception of band 2 with $\Delta z = 0.47$. A more realistic treatment would have to take into account the frequency dependence of the noise temperatures of both experiments, and the different dish and receiver types of SKA1. However, we expect this to have a negligible effect on our results.

Following Battye et al. (2013) and Bull et al. (2015) for the intensity mapping noise calculations, we calculate the single dish noise for SKA1-MID as

$$N_\ell^{\rm SD} = \sigma_{\rm pix}^2 \Omega_{\rm pix} W_\ell^{-1}. \tag{19}$$

Here, we use the solid angle per pixel $\Omega_{\rm pix} = 4\pi f_{\rm sky}/N_{\rm pix}$, the number of pixels $N_{\rm pix}$, the beam ($\Theta_{\rm FWHM}$) smoothing function $W_\ell = \exp\left(-\ell^2\Theta_{\rm FWHM}^2/(8\ln 2)\right)$, the pixel noise $\sigma_{\rm pix} = T_{\rm sys}\sqrt{N_{\rm pix}/(t_{\rm tot}\delta_\nu N_{\rm dish})}$, and the frequency resolution (channel width) δ_ν.

For HIRAX, we calculate the interferometer noise

$$N_\ell^{\rm INT} = \frac{(\lambda^2 T_{\rm sys})^2}{2A_{\rm e}^2 d\nu\, n(u) t_{\rm p}}, \tag{20}$$

with the frequency bin width $d\nu$, the time per pointing $t_{\rm p} = t_{\rm tot}/N_{\rm p}$, the effective collecting area of one dish $A_{\rm e} = (D_{\rm dish}/2)^2\pi$, and using the relation $u = \ell/(2\pi)$ for the baseline density $n(u)$.

For all experiments we assume full survey overlap with LSST.

3.2 Photometric galaxy counts

We normalize the LSST sample to be a total of $\sim 6.3 \times 10^9$ galaxies at $m^* = 27$.[1] The galaxy shot noise for LSST is calculated as $C^{\rm shot} = 4\pi/N_{\rm g}^{\rm LSST}(z)$, where we use a fitting function to calculate the number of detected galaxies in the considered redshift bin, $N_{\rm g}^{\rm LSST}$ (equations 8 and 11). We consider all possible LSST redshift bins to have their upper edge at the same $z_{\rm max}^{\rm LSST} = 3.9$, and the lower bin edge at a separation from the upper edge of the foreground bin, $z_i^{\rm fg} + 0.1$. The choice of a separation of $\Delta z = 0.1$ might not completely rule out cross correlations (because of photometric redshift outliers), but should be enough to reduce them to a very low level. We calculate the number count slope for LSST using an adjusted version of the code provided in Alonso et al. (2015) to extend to more stringent luminosity cutoffs m^*. We then interpolate $(5s_{\rm g} - 2)n_{\rm g}$ on a fine grid (z and m^*) to speed up the numerical calculations.

[1]This is slightly more conservative than the number quoted in LSST Science Collaboration (2009), i.e. almost 10^{10} galaxies for $m^* = 27.5$.

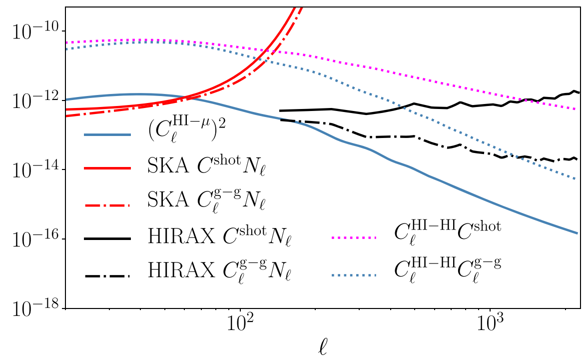

Figure 5. All contributions to $\Delta C_\ell^{\rm HI-\mu}$ as in equation (21), for a foreground redshift bin from $z = 0.85$ to 1.35 and a background bin $z \geq 1.45$. The common factor of $2/((2\ell + 1)\Delta\ell f_{\rm sky}$ was omitted here. Terms proportional to the SKA1-MID (HIRAX) noise are plotted in red (black) and terms proportional to shot noise and cosmic variance are plotted cyan and steel blue, respectively. For this choice of binning, the H I intensity mapping noise is subdominant, followed by pure cosmic variance, but both dominated by terms with shot noise, the biggest source of error. Note that the choice of intermediate foreground and background redshift in this plot is only to ease comparison, but not necessarily ideal for magnification measurements.

In order to illustrate the different error contributions and consolidate our findings, Fig. 5 shows all summands contributing to the H I-magnification cross-correlation error:

$$\left(\Delta C_\ell^{\rm HI-\mu}\right)^2 = \frac{2}{(2\ell+1)\Delta\ell f_{\rm sky}}\left(\left(C_\ell^{\rm HI-\mu}\right)^2 + C_\ell^{\rm g-g}C_\ell^{\rm HI-HI} + C^{\rm shot}C_\ell^{\rm HI-HI} + N_\ell C_\ell^{\rm g-g} + C^{\rm shot}N_\ell\right). \tag{21}$$

The amplitude of the different contributions here depends on the choice of experiments and redshift binning.

To ease comparison we used the same single redshift bin for HIRAX and SKA1-MID in Fig. 5, from $z = 0.85$ to 1.35. For HIRAX a magnitude cutoff of $m^* = 24.4$ maximizes the signal-to-noise ratio; for SKA1-MID it is 24.3. This optimization will be discussed further in Section 4.1. In this case shot noise dominates the error throughout, but it becomes comparable to cosmic variance (mostly $C_\ell^{\rm g-g}C_\ell^{\rm HI-HI}$) on large scales for SKA1-MID. Note that small scales are practically inaccessible for SKA1-MID due to its poor angular resolution, restricting it to much larger scales than HIRAX.

The multipole resolution is set by the maximum scale accessible by the SKA, i.e. the survey area $S_{\rm area}$ when in single dish mode. We estimate $\ell_{\rm min}^{\rm SKA} = 2\pi/\sqrt{S_{\rm area}} \sim 3$, but choose a more conservative value of $\ell_{\rm min}^{\rm SKA} = 10$ for the Limber approximation to hold (Loverde & Afshordi 2008). For the HIRAX interferometer it is set by the field of view (fov) which depends on frequency. For the sake of simplicity we ignore this dependence and assume a mean fov = 35.5 deg^2 (Newburgh et al. 2016), giving $\ell_{\rm min}^{\rm HIRAX} = 2\pi/\sqrt{\rm fov} \sim 60$. From the signal-to-noise ratio $C_\ell^{\rm HI-\mu}/\Delta C_\ell^{\rm HI-\mu}$ we calculate the cumulative (total) signal to noise as

$$\mathrm{SN}_{\rm tot} = \sqrt{\sum_{\bar\ell=\ell_{\rm min}}^{\ell}\left(C_{\bar\ell}^{\rm HI-\mu}/\Delta C_{\bar\ell}^{\rm HI-\mu}\right)^2}, \tag{22}$$

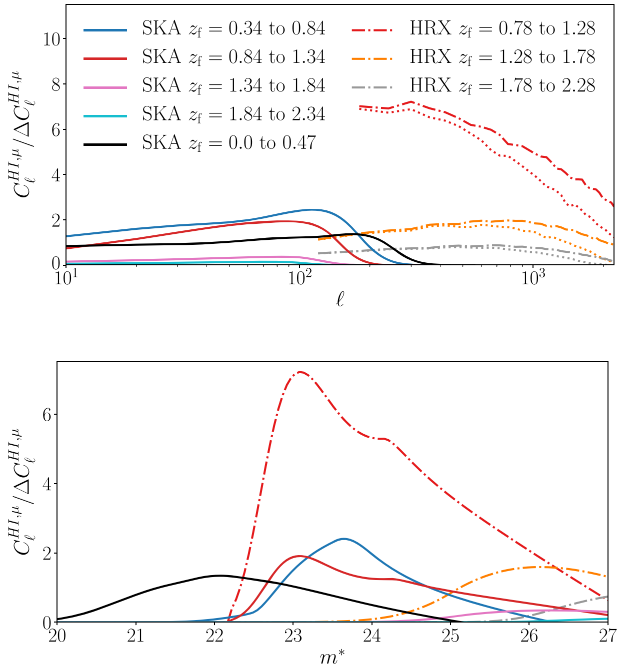

Figure 6. *Upper panel:* The expected signal-to-noise ratio of the magnification signal for the combinations HIRAX 1024 (dotted-dashed lines), HIRAX 512 (dotted lines) and SKA1 band 1 (solid lines) and band 2 (solid black line) with LSST. We use different foreground redshift bins, always combined with one single non-overlapping background bin. Shot noise largely dominates, therefore the 512 dish version of HIRAX performs surprisingly well compared to the full array with 1024 dishes. *Lower panel:* The optimization of the signal-to-noise ratio as a function of magnitude cutoff m^*. This panel is for single ℓ bins only, for SKA1-MID $\ell = 80$ and for HIRAX $\ell = 200$. These values were chosen to lie within the experiment's range of maximum sensitivity.

where the sum runs over the relevant ℓ values, with the minimum ℓ, and the binning $\Delta\ell$, set by $\ell_{\rm min}$. We note, however, that the cumulative signal-to-noise ratio $\mathrm{SN}_{\rm tot}$ is binning independent.

4 RESULTS AND DISCUSSION

4.1 Signal-to-noise ratio

We maximize the signal-to-noise ratio with respect to the galaxy magnitude threshold m^* for each H I survey and redshift bin. We consider an optimization range of $m^* \in [19, 27]$ and plot $\mathrm{SN}(m^*)_{\rm tot}$ for a few examples in Fig. 6. The optimal values we found (using the *python* package *scipy optimize*) are shown in Table 1. Generally, for low-redshift foreground bins, also a low m^* is preferred, which increases the number count slope at the acceptable cost of increasing the (negligible) shot-noise at these redshifts. For high-redshift foreground bins, however, shot-noise increases and m^* needs to be higher to account for this.

Fig. 6 shows the optimized signal to noise as a function of multipole for all considered experiment and redshift combinations. Maps in each foreground redshift bin are correlated with one single redshift bin of LSST, separated from the foreground by $\Delta z = 0.1$ and ranging up to $z = 3.9$. Low redshift foreground bins benefit from a wider background sample containing a larger number of galaxies. Therefore, they often perform better than high redshift bins, especially in the case for HIRAX. The sensitivity of HIRAX

Table 1. Optimized magnitude cutoffs, m^*, as well as cumulative signal-to-noise values for all experiments and redshift bins. Individual redshift bins of HIRAX are better than SKA1-MID also due to the higher number of ℓ bins that contribute.

	SKA1 B1	–	–	–
z range	0.34–0.84	0.84–1.34	1.34–1.84	1.84–2.34
m^*	23.6	23.1	26.3	27.0
$\mathrm{SN}_{\rm tot}$	8.7	6.3	1.1	0.4
	HIRAX	–	–	SKA1 B2
z range	0.78–1.28	1.28–1.78	1.78–2.28	0.0–0.47
m^*	23.0	26.1	27.0	22.1
$\mathrm{SN}_{\rm tot}$	28.5	9.4	3.8	5.8

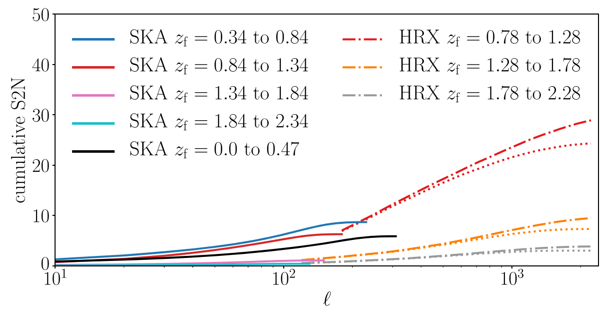

Figure 7. This plot shows the cumulative signal-to-noise ratio, equation (22). For HIRAX especially, the error is dominated by the galaxy shot noise. Therefore even the down-scaled design with 512 dishes yields very similar results compared to the full proposal with 1024 dishes.

is best at comparably small scales, where the power spectrum drops $\sim\ell^2$ (see e.g. Fig. 3). The shot noise, however, becomes the dominant error on smaller scales. The 512 dish design for HIRAX performs surprisingly well, as even in this case the interferometer noise remains subdominant.

Fig. 7 shows the cumulative signal to noise which reaches levels of $\sim$30 for individual redshift bins. The performance of SKA1-MID and HIRAX is similar for single ℓ bins, but HIRAX covers a larger multipole range. Both experiments yield best results at intermediate redshifts of $0.6 < z < 1.3$. As they are sensitive to different angular scales, most of their constraining power can be combined.

4.2 Weighting analysis

In this section we will investigate whether it is possible to further increase the signal-to-noise ratio by using the weighting proposed by Bartelmann & Schneider (2001). Let us suppose that galaxies are split into magnitude bins. We can then consider a weighted galaxy overdensity $\sum_i \mathcal{W}_i \delta_{{\rm g},i}$, where summation runs over galaxy magnitude bins and $\mathcal{W}_i$ denotes a scale-independent weighting function.

In Fourier space, we can derive the weighted signal-to-noise ratio, $(\mathrm{SN}_\mathcal{W})$, adapting the formula derived in Yang & Zhang (2011) for a 21cm intensity mapping foreground sample. We can then write the total signal-to-noise ratio as:

$$(\mathrm{SN}_\mathcal{W})^2 = \sum_\ell \frac{(\ell + 1/2)\Delta\ell f_{\rm sky}}{1 + \left(C_\ell^{\rm HI-HI} + N_\ell\right) \frac{\langle b_{\rm g}\mathcal{W}\rangle^2 C_\ell^{\rm DM,b} + \langle\mathcal{W}\rangle^2 C^{\rm shot}}{\left\langle C_\ell^{\rm HI-\mu}\mathcal{W}\right\rangle^2}}, \quad (23)$$

where the average of a quantity x weighted by the number of galaxies $N_{{\rm g},i}$ per magnitude bin m_i is denoted as $\langle x\rangle = \sum_i x(m_i) N_{{\rm g},i} / \sum_i N_{{\rm g},i}$.

Table 2. Cumulative signal-to-noise ratio derived using the weighted galaxy overdensity described in Section 4.2. Not requiring a magnitude cut, this method gives best results as all available galaxies are used. We also present the forecasted fractional errors on the $\Omega_{\rm HI}b_{\rm HI}$. Note that we fix all other cosmological parameters when calculating these constraints.

	SKA1 B1	–	–	–
z range	0.34–0.84	0.84–1.34	1.34–1.84	1.84–2.34
$\mathrm{SN}_{\mathcal{W}}$	16.0	7.1	2.6	0.7
$\frac{\delta(\Omega_{\rm HI}b_{\rm HI})}{(\Omega_{\rm HI}b_{\rm HI})}$	0.06	0.14	0.38	1.4
	HIRAX	–	–	SKA1 B2
z range	0.78–1.28	1.28–1.78	1.78–2.28	0.0–0.47
$\mathrm{SN}_{\mathcal{W}}$	57.5	21.5	6.3	18.8
$\frac{\delta(\Omega_{\rm HI}b_{\rm HI})}{(\Omega_{\rm HI}b_{\rm HI})}$	0.02	0.05	0.16	0.05

We also note that the dark matter power spectrum in the background is given by $C_\ell^{\rm DM,b}(z) = H_0/c \int {\rm d}z E(z)(W/r)^2 P_{\rm m}((\ell+1/2)/r, z)$.

We utilize the weighting function from Bartelmann & Schneider (2001), $\mathcal{W} = (5s_{\rm g} - 2)/2$, but we note that in Yang & Zhang (2011) this weight is generalized to include scale dependence. This can further improve the overall signal-to-noise ratio (especially for cases where the shot noise is low), but here we use the simplest version that is sufficient for conservative forecasting.

We present the results using this approach in Table 2. They offer an improvement over the results from subsection 4.1 up to a factor of 3 in the cumulative signal-to-noise ratio, depending on the foreground redshift. This is expected as this method boosts the signal and uses all available galaxies, keeping the shot noise to a minimum – we will discuss this further in our conclusions (Section 5). We now proceed to present forecasts for H I parameters.

We now discuss what can be learned about the combination of H I abundance and bias, $\Omega_{\rm H\,I}b_{\rm H\,I}$, from the expected measurements. These parameters are very important for galaxy evolution studies but remain poorly constrained (Crighton et al. 2015). Intensity mapping is a unique and very effective way to provide unprecedented constraints on H I parameters across a wide redshift range. For forecasts using H I clustering in auto and cross correlation with optical galaxy surveys we refer the reader to (Pourtsidou, Bacon & Crittenden 2017).

Arguably, the detections we are presenting here are not expected to be competitive with forthcoming cosmic shear measurements with regards to cosmological parameter constraints. In addition, H I parameters are degenerate with cosmological parameters. Hence, the best use of this data when they become available (at least in the first instance) would be to keep the cosmology fixed and focus on measuring the H I parameters. This gives the $\Omega_{\rm H\,I}b_{\rm H\,I}$ fractional error simply as:

$$\frac{\delta(\Omega_{\rm HI}b_{\rm HI}(z))}{\Omega_{\rm HI}b_{\rm HI}(z)} = 1/\mathrm{SN}_{\mathcal{W}}. \tag{24}$$

Our derived H I constraints are summarized in Table 2. As an example, for our highest signal-to-noise ratio $\mathrm{SN}_{\mathcal{W}} = 51.6$ at $z \simeq 1$ we get a ~ 2 per cent error, which is much better than currently available measurements at this redshift (Crighton et al. 2015). We emphasize that these constraints assume all cosmological parameters fixed. This is common in H I intensity mapping forecasts, see e.g. Bacon et al. (2020). Although the latest constraints on the standard six parameter cosmological model are about 1 per cent for each parameter (Aghanim et al. 2018), this can still have an impact on the constraints we provided because there are strong degeneracies. This is particularly relevant when constraints on $\Omega_{\rm H\,I}b_{\rm H\,I}$ reach below the 10 per cent level. It will be interesting to account for this by performing a Fisher matrix analysis in future work.

5 CONCLUSIONS

In this paper we proposed the use of H I intensity maps from large sky surveys with forthcoming radio arrays in cross correlation with background optical galaxy samples from Stage IV photometric surveys, in order to detect the cosmic magnification signal.

We then derived predictions for the signal-to-noise ratio of the magnification signal from the foreground H I maps acting on background galaxies using two distinct methods. For both we considered the survey combinations HIRAX with LSST and SKA1-MID with LSST. In 4.1 the signal-to-noise was optimized by changing the galaxy magnitude threshold m^* for LSST, since a lower magnitude cutoff boosts the magnification signal. Due to their different resolutions and mode operations, the information provided by the HIRAX interferometer is complementary to the data gathered by SKA1-MID in autocorrelation (single dish) mode.

Then, in subsection 4.2, we presented a different approach that significantly improves the expected detections in low-redshift bins by using a weighted galaxy overdensity. This method allows us to always use all detectable galaxies and thus keeps shot noise at a minimum, whereas the method described in 4.1 requires magnitude cutoffs in the galaxy samples. The lower the foreground redshift, the more stringent these optimized cuts and thus the difference between both approaches increases. When the galaxy samples in the weighted summation are restricted to the same magnitude cuts as in 4.1, the forecasts of both methods agree better.

A detection seems likely with forecasted cumulative signal-to-noise ratios in the range of $\sim$50, but a more detailed analysis with appropriate simulations will be needed to fully assess all relevant sources of errors, e.g. foreground contamination residuals and cleaning effects. Foreground residuals are not expected to be significant in the cross-correlation between H I intensity maps and galaxies. The loss of long-wavelength radial modes in the H I data is also not expected to have a significant deteriorating effect on this observable. Foreground contamination is expected to be most severe on large angular scales, as shown in e.g. Wolz et al. (2014), Cunnington et al. (2019b). We assessed the sensitivity of our analysis to this by entirely discarding the lowest three ℓ bins (i.e. $\ell < 40$ for SKA and $\ell < 240$ for HIRAX). Even with the very pessimistic assumption that no information can be obtained from these bins, the signal-to-noise ratio is only reduced by $\sim$3 per cent and $\sim$6 per cent for HIRAX and SKA, respectively. However, it would be useful to properly account and quantify all foreground effects by extending the cross-correlation simulations studies performed in Witzemann et al. (2019), Cunnington et al. (2019b,a) – we leave this for future work. We also note that the choice of redshift binning could be reconsidered to make the analysis more realistic for a foreground cleaned H I survey. Furthermore, using realistic simulated LSST catalogues we can implement and test the performance of scale-dependent optimal weighting functions (Yang & Zhang 2011).

Finally, we turned the expected signal-to-noise ratio into a fractional constraint on $\Omega_{\rm H\,I}b_{\rm H\,I}(z)$. These H I parameters are still poorly constrained, but we show that a cosmic magnification analysis can yield a fractional error as good as $\sim$2 per cent, if cosmological parameters are fixed.

To conclude, both methods presented in this work give results suggesting that it will certainly be possible to detect the magnification signal once the data are available. This will be complementary to measurements using optical foreground samples with completely different systematics.

ACKNOWLEDGEMENTS

We are extremely grateful to the anonymous referee, whose suggestions greatly improved the quality and scope of this manuscript. We thank David Bacon for useful discussions. AW and MGS acknowledge support from the South African Square Kilometre Array Project and National Research Foundation (Grant No. 84156). AP is a UK Research and Innovation Future Leaders Fellow, grant MR/S016066/1, and also acknowledges support from the UK Science & Technology Facilities Council through grant ST/S000437/1.

REFERENCES

Abate A. et al., 2012, preprint (arXiv:1211.0310)
Abbott T. et al., 2016, MNRAS, 460, 1270
Aghanim N. et al., 2018, preprint (arXiv:1807.06209)
Alonso D., Bull P., Ferreira P. G., Maartens R., Santos M. G., 2015, ApJ, 814, 145
Amendola L. et al., 2018, Living Rev. Rel., 21, 2
Bacon D. J., Refregier A. R., Ellis R. S., 2000, MNRAS, 318, 625
Bacon D. J. et al., 2020, PASA, 37, e007
Bartelmann M., Schneider P., 2001, Phys. Rep., 340, 291
Battye R. A., Browne I. W. A., Dickinson C., Heron G., Maffei B., Pourtsidou A., 2013, MNRAS, 434, 1239
Bernstein G., Jain B., 2004, ApJ, 600, 17
Bonvin C., Durrer R., 2011, Phys. Rev., D84, 063505
Bull P., Ferreira P. G., Patel P., Santos M. G., 2015, ApJ, 803, 21
Crighton N. H. M. et al., 2015, MNRAS, 452, 217
Cunnington S., Harrison I., Pourtsidou A., Bacon D., 2019a, MNRAS, 482, 3341
Cunnington S., Wolz L., Pourtsidou A., Bacon D., 2019b, MNRAS, 488, 5452
Duncan C., Joachimi B., Heavens A., Heymans C., Hildebrandt H., 2014, MNRAS, 437, 2471
Gabasch A. et al., 2006, A&A, 448, 101
Garcia-Fernandez M. et al., 2018, MNRAS, 476, 1071
Hall A., Bonvin C., Challinor A., 2013, Phys. Rev. D, 87, 064026
Heymans C. et al., 2012, MNRAS, 427, 146
Hildebrandt H., van Waerbeke L., Erben T., 2009, A&A, 507, 683
Hui L., Gaztañaga E., Loverde M., 2007, Phys. Rev. D, 76, 103502
Jain B., Taylor A., 2003, Phys. Rev. Lett., 91, 141302
Jalilvand M., Majerotto E., Durrer R., Kunz M., 2019, J. Cosmol. Astropart. Phys., 1901, 020
Kaiser N., Wilson G., Luppino G. A., 2000, preprint (astro-ph/0003338)
Kilbinger M., 2015, Rep. Prog. Phys., 78, 086901
Lewis A., Challinor A., Lasenby A., 2000, ApJ, 538, 473
Limber D. N., 1954, ApJ, 119, 655
Loverde M., Afshordi N., 2008, Phys. Rev. D, 78, 123506
Loverde M., Hui L., Gaztañaga E., 2007, Phys. Rev. D, 75, 043519
LSST Science Collaboration, 2009, preprint (arXiv:0912.0201)
Mandelbaum R., 2018, Ann. Rev. Astron. Astrophys., 56, 393
Menard B., Bartelmann M., 2002, Astron. Astrophys., 386, 784
Menard B., Scranton R., Fukugita M., Richards G., 2010, MNRAS, 405, 1025
Newburgh L. B. et al., 2016, in Hall H. J., Gilmozzi R., Marshall H. K., eds, Ground-based and Airborne Telescopes VI, SPIE, p. 99065X
Pourtsidou A., Metcalf R. B., 2014, MNRAS, 439, L36
Pourtsidou A., Bacon D., Crittenden R., 2017, MNRAS, 470, 4251
Santos M. et al., 2015, Advancing Astrophysics with the Square Kilometre Array (AASKA14), p. 19, Available at: http://pos.sissa.it/cgi-bin/reader/conf.cgi?confid=215
Santos M. G. et al., 2017, preprint (arXiv:1709.06099)
Schechter P., 1976, ApJ, 203, 297
Scranton R. et al., 2005, ApJ, 633, 589
Smith R. E. et al., 2003, MNRAS, 341, 1311
Takahashi R., Sato M., Nishimichi T., Taruya A., Oguri M., 2012, Astrophys. J., 761, 152
Taylor A. N., Kitching T. D., Bacon D. J., Heavens A. F., 2007, MNRAS, 374, 1377
van Uitert E. et al., 2018, MNRAS, 476, 4662
van Waerbeke L. et al., 2000, Astron. Astrophys., 358, 30
Van Waerbeke L., Hildebrandt H., Ford J., Milkeraitis M., 2010, Astrophys. J., 723, L13
Wittman D. M., Tyson J. A., Kirkman D., Dell'Antonio I., Bernstein G., 2000, Nature, 405, 143
Witzemann A., Alonso D., Fonseca J., Santos M. G., 2019, MNRAS, 485, 5519
Wolz L., Abdalla F. B., Blake C., Shaw J. R., Chapman E., Rawlings S., 2014, MNRAS, 441, 3271
Yang X., Zhang P., 2011, MNRAS, 415, L45
Zahn O., Zaldarriaga M., 2006, Astrophys. J., 653, 922
Zhang P., Pen U.-L., 2006, MNRAS, 367, 169
Ziour R., Hui L., 2008, Phys. Rev. D, 78, 123517

This paper has been typeset from a TEX/LATEX file prepared by the author.